Project Report
TIP-86

Computational Modeling of Additive Manufacturing by Power Bed Laser Fusion: FY18 Engineering Research Technical Investment Program

E.M. Parsons

30 January 2019

Lincoln Laboratory
MASSACHUSETTS INSTITUTE OF TECHNOLOGY
LEXINGTON, MASSACHUSETTS

This material is based upon work supported by the United States Air Force under Air Force Contract No. FA8702-15-D-0001.

This report is the result of studies performed at Lincoln Laboratory, a federally funded research and development center operated by Massachusetts Institute of Technology. This material is based upon work supported by the United States Air Force under Air Force Contract No. FA8702-15-D-0001. Any opinions, findings, conclusions or recommendations expressed in this material are those of the author(s) and do not necessarily reflect the views of the United States Air Force.

Massachusetts Institute of Technology
Lincoln Laboratory

Computational Modeling of Additive Manufacturing by Power Bed Laser Fusion: FY18 Engineering Research Technical Investment Program

E.M. Parsons

Group 74

Project Report TIP-86

30 Janaury 2019

Lexington Massachusetts

This page intentionally left blank.

TABLE OF CONTENTS

This page intentionally left blank.

LIST OF FIGURES

LIST OF FIGURES
(Continued)

1. INTRODUCTION TO ADDITIVE MANUFACTURING BY SELECTIVE LASER MELTING

Additive manufacturing (AM) or "3D printing" has had a huge impact on numerous sectors at scales ranging from microfabrication to big area manufacturing (size of meters). Many predict that it will soon be recognized as the technology behind the third industrial revolution. It is defined by the ISO/ASTM as "the process of joining materials to make parts from 3D model data, usually layer upon layer, as opposed to subtractive and formative manufacturing methodologies." With additive manufacturing, parts of complex geometry can be built with a single machine operation and without any special masks, tooling, dies, or fixtures. Originally used primarily for fabrication of prototypes and models of design concepts, various additive manufacturing methods are presently capable of producing functional devices, components, and structures constructed from numerous types of materials.

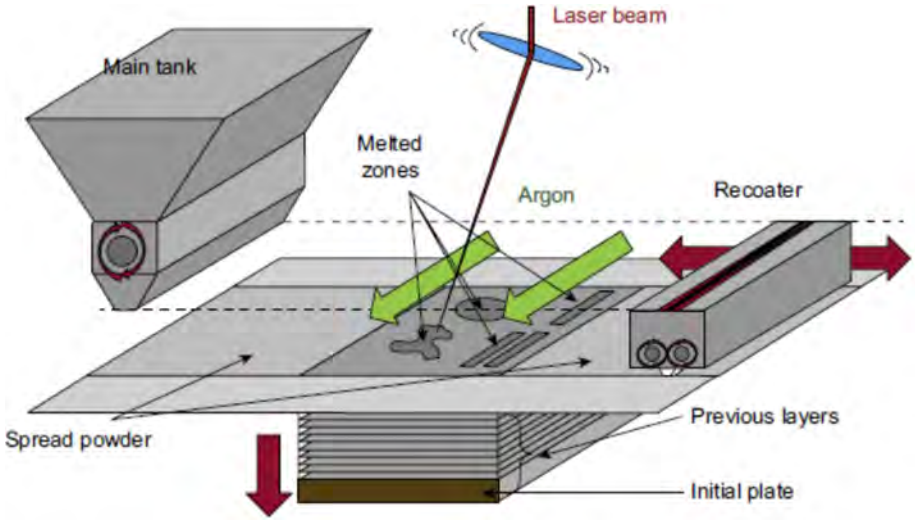

Figure 1. Schematic of the build chamber of a selective laser melting machine, showing the laser beam, build plate, powder recoater, and flow of inert gas. This example uses a hopper to deposit powder (top left), similar to the design of the micro-SLM.

MIT LL is increasingly using the AM process selective laser melting (SLM) to build metal structural components for prototypes. The highest resolution form of metal printing, SLM is a powder bed fusion process in which selective areas of a bed of metal powder are fully melted and consolidated with a high energy laser (Figure 1). Once fusion of a given layer is complete, the build platform is lowered, and another layer is spread or "recoated" over the platform. SLM is ideal for production of the low volumes of high value parts that are typical of the defense and

aerospace sectors. Heavily light-weighted parts and parts with internal channels or cavities can be manufactured, sometimes reducing to a single piece an assembly that would otherwise consist of dozens of separate components joined together. In many cases, SLM enables fabrication of parts with complex features that could not be produced at all with conventional methods.

Despite the great potential of SLM to improve performance and reduce lead times, SLM alloy properties, part quality, and process reliability must improve for SLM to become broadly used in critical structural applications. Two shortcomings prevent SLM from gaining widespread adoption. First, part quality and performance are functions of the part geometry and build orientation. Because the understanding of the relationships between process parameters, fused material properties and part performance is limited, process parameters developed for prismatic samples can result in defects, warping, uncertain material properties, and residual stresses. Second, processing by SLM is presently limited to just a handful of alloys that exhibit unremarkable mechanical properties. For example, the only aluminum alloys commonly used with SLM are AlSi10Mg and Al12Si. These alloys were designed specifically for casting and exhibit yield strength, ductility, and fatigue strength substantially inferior to the properties of frequently used wrought alloys such as aluminum 2024, 6061, and 7075. Development of new alloys for AM typically entails numerous experimental trials, with process parameters selected by trial and error, requiring many years and costing tens of millions of dollars or more.

2. MOTIVATION: THE NEED FOR MATHEMATICAL MODELS OF SLM

Laser consolidation by SLM is exceptionally complex because it involves multiple types of physics and numerous process parameters. The physics include phase changes, mass transfer, and several modes of heat transfer (Figure 2a). The process parameters include both laser parameters (beam diameter, velocity, and scan pattern) and powder bed parameters (layer thickness, packing density, absorptivity, conductivity, and initial temperature), as illustrated in Figure 2b. All these parameters combined determines the consolidated material properties and part performance.

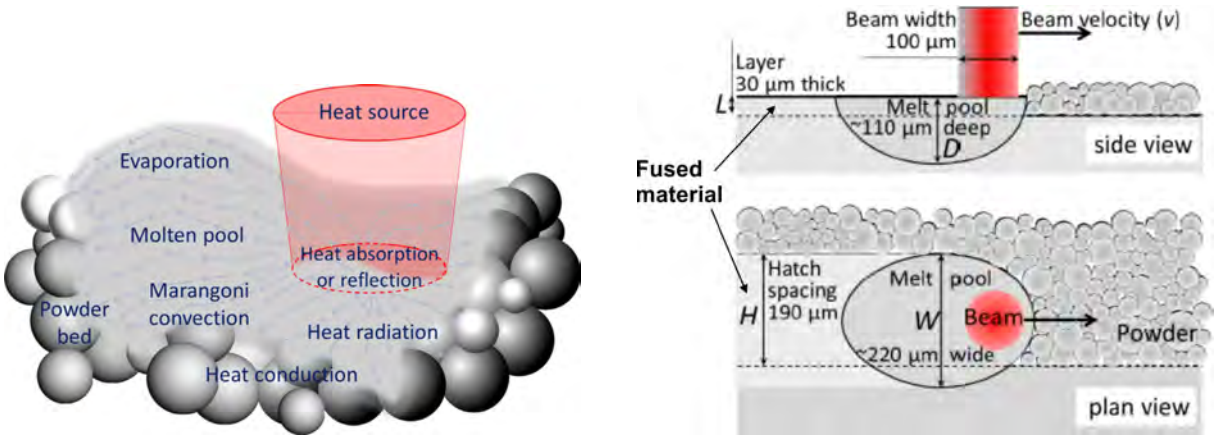

(a) (b)

Figure 2. Schematics of laser heating and melt pool formation during SLM: (a) Multiple types of heat transfer occur simultaneously; (b) SLM process parameters include beam size, beam velocity, powder layer thickness, and hatch spacing.

In this program, we are developing physics-based modeling and simulation capabilities that will be used to optimize SLM process parameters and to design new alloys for SLM. Predictive modeling is needed to relate the numerous process parameters to the local melt pool characteristics and thermal history that produce the desired microstructures, material properties, and part performance. By controlling melt pool temperature and aspect ratio, we can prevent defects due to lack of fusion (energy too low), keyholing, evaporation of alloying elements (energy too high), and balling of the melt pool (scan velocity too high). At the level of microstructure, local thermal gradients, solidification velocities, and cooling rates can be manipulated to engineer grain type, size, and orientation. Finally, residual stresses that cause defects, warping, and poor part performance can be reduced by designing scan strategies that produce uniform heating and cooling.

In one application, these computational tools will be used to tune process parameters based on the geometry of the part. Process parameters determined experimentally are strictly only valid for the geometry of the test samples. In an actual part, thermal conditions and strains vary with location, potentially causing defects and the development of residual stresses that can reduce dimensional accuracy and lead to failure during the build or in the field. Optimal process parameters, specific to the geometry of the part being built, can only be systematically determined by physically motivated simulation of the melting and consolidation processes.

In the second application, the computational tools will be used to optimize material microstructure and properties—for both improving the processing of existing SLM alloys and developing new alloys for SLM. While the yield strength, fatigue strength, and toughness of existing SLM alloys are typically inferior to those of their wrought counterparts, the properties of alloys designed specifically for the thermal cycling and high cooling rates of SLM have the potential to match or exceed those of wrought alloys. Simulation will provide detailed knowledge of the material's thermal history during SLM, including cooling rates, temperature gradients, and solidification velocities. These process conditions, together with the material's elemental composition, can then be designed to control the grain morphology and formation of phases, while also preventing loss of alloying elements and material defects such as the solidification cracking that frequently occurs in high-alloy metals. For example, disrupting the formation of columnar grains and promoting the formation of equiaxed, fine grained microstructures can enhance fatigue strength and prevent hot tearing during solidification.

3. GOVERNING EQUATIONS OF LASER CONSOLIDATION

The laser beam, with radius r, moves at constant velocity v in the x-direction as it scans over the surface of the powder bed, which lies in the $(x,\, y)$ plane (Figure 3). It is represented by a Gaussian intensity distribution in the $(x,\, y)$ plane,

$$I(x, y, t) = \frac{A \cdot P}{\sigma\, \pi\, r^2} \exp\left(-\frac{(x - v\, t)^2 + y^2}{\sigma\, r^2} \right) \equiv I_0 \exp\left(-\frac{(x - v\, t)^2 + y^2}{\sigma\, r^2} \right), \tag{1}$$

where P is the power of the laser beam at the surface of the powder bed, A is the absorptivity of the powder, I_0 is the peak intensity of the beam, and σ describes the shape of the intensity distribution (Figure 4). For most SLM machines, r is measured at the position where the intensity of the beam has fallen to $1/\mathrm{e}^2$ of its maximum intensity, and therefore $\sigma = 2$. Assuming that the heat transfer is dominated by thermal conduction, the heat diffusion equation can be written as

$$\rho\, c_p \frac{\partial T}{\partial t} - \mathrm{Div}\,(k\, \mathrm{Grad}\, T) = I\,(x,\, y)\, \delta\,(z)\,, \tag{2}$$

where $\rho = \rho(T)$ is the mass density, $c_\mathrm{p} = c_\mathrm{p}(T)$ is the specific heat capacity, $k = k(T)$ is the thermal conductivity, and $\delta\,(z)$ is a delta function at the surface of the powder bed. The mechanical problem is described by balance of linear momentum written in the reference configuration,

$$\rho \frac{\partial^2 \mathbf{u}}{\partial t^2} - \mathrm{Div}\sigma = 0, \tag{3}$$

where $u = u(\mathbf{X}, t)$ is the displacement vector, and $\sigma = \sigma(\mathbf{X}, t)$ is the Cauchy stress tensor.

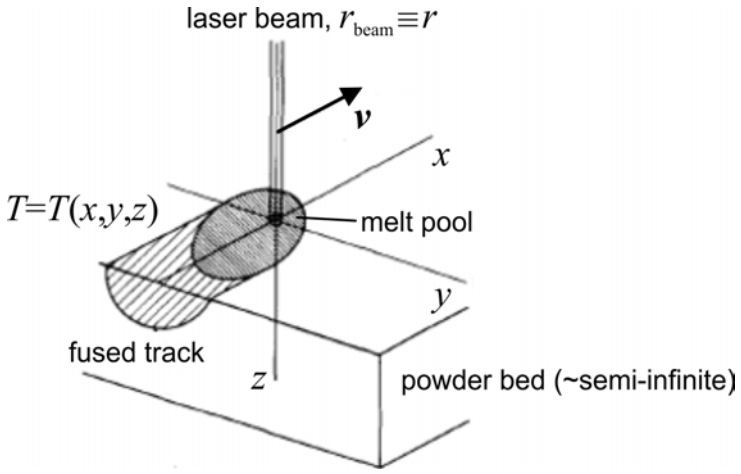

Figure 3. Schematic of the modeling of the laser fusion process. The laser beam moves at constant velocity in the x-direction, and the powder bed is approximated as semi-infinite. The model predicts the steady temperature distribution that moves with the beam at velocity $\mathbf{v}$.

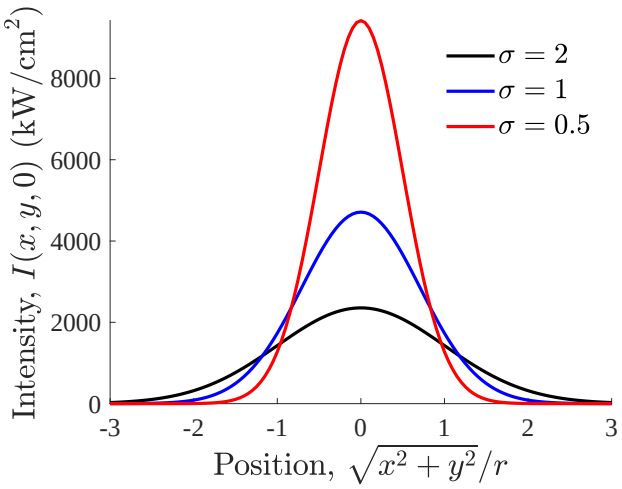

Figure 4. Profile of the laser beam intensity as a function of the radial position for various values of σ*, the beam shape parameter.*

4. ANALYTICAL MODELING OF LASER CONSOLIDATION

With the benefit of several modeling assumptions, we derived the analytical solution for the steady state temperature distribution generated by a scanning Gaussian intensity source. This analytical model serves two purposes: First, it identifies simple nondimensional groups of process parameters and material properties that affect the properties of the consolidated material. Second, it acts as a benchmark for the more complex numerical models of Section 5, verifying many aspects of the numerical methods.

We model the powder bed as semi-infinite and approximate the material properties to be independent of temperature. At steady state, the heat equation can be solved for $t = 0$, when the laser beam is at $x = 0$, by superimposing the Gaussian intensity distributions that occurred at earlier times $t' = 0 \rightarrow -\infty$ when the beam was located at coordinates (x', y'). The solution is found by by a standard Green's function method and then integrated analytically over x' and y'. Transformation to dimensionless variables results in

$$T(x, y, z) - T_0(x, y, z) = \frac{A \cdot P}{k\, r} \int_0^\infty \frac{\exp(-H)}{\sqrt{\sigma}\pi^{3/2}(1+u^2)} \mathrm{d}u, \tag{4}$$

with

$$H = H\left(\frac{x}{r}, \frac{y}{r}, \frac{z}{r}, \frac{v\, r}{\alpha}, \sigma, u\right), \tag{5}$$

in which u is a dimensionless function of $t'' \equiv -t'$. The solution therefore takes the form of an amplitude term that does not vary with position multiplied by a dimensionless shape function:

$$T(x, y, z) - T_0(x, y, z) = \underbrace{\frac{A \cdot P}{k\, r}}_{\text{dimension } T} \times \underbrace{f\left(\frac{x}{r}, \frac{y}{r}, \frac{z}{r}, \frac{v\, r}{\alpha}, \sigma\right)}_{\text{dimensionless shape function}}. \tag{6}$$

The amplitude term increases with increasing absorbed power and decreases with increasing thermal conductivity and beam size. The shape function, f, depends only on the shape of the beam's intensity profile and the dimensionless velocity, $\overline{v} \equiv v\, r/\alpha$, where $\alpha = k/\rho c_\mathrm{p}$ is the thermal diffusivity. The dimensionless velocity, also known as the Péclet number, characterizes the ratio of heat flow by transport to heat flow by diffusion. For a given thermal conductivity and beam intensity, f completely determines the distribution of temperature in the material. Similarly, a dimensionless group describing the power that is required for the laser melting of metals can be defined by dividing the amplitude term by the temperature rise: $\overline{P} \equiv \frac{A \cdot P}{k\, r} \frac{1}{(T_\mathrm{m} - T_0)}$.

We numerically integrate Equation 4 and evaluate the shape function along each of the coordinate axes to determine the maximum temperature in the material and explore the shape of the temperature distribution as a function of the dimensionless velocity (Figure 5). As expected, in the y and z directions, the temperature is a maximum at the center of the beam and at the surface of the material ($y = 0$, $z = 0$). However, in the x-direction, the maximum temperature shifts further

behind the center of the beam as $\overline{v}$ increases (Figure 5a). As the beam velocity increases, the time for heat flow by conduction decreases, and the effect of heat input at prior times and locations begins to dominate over the effect of thermal conduction.

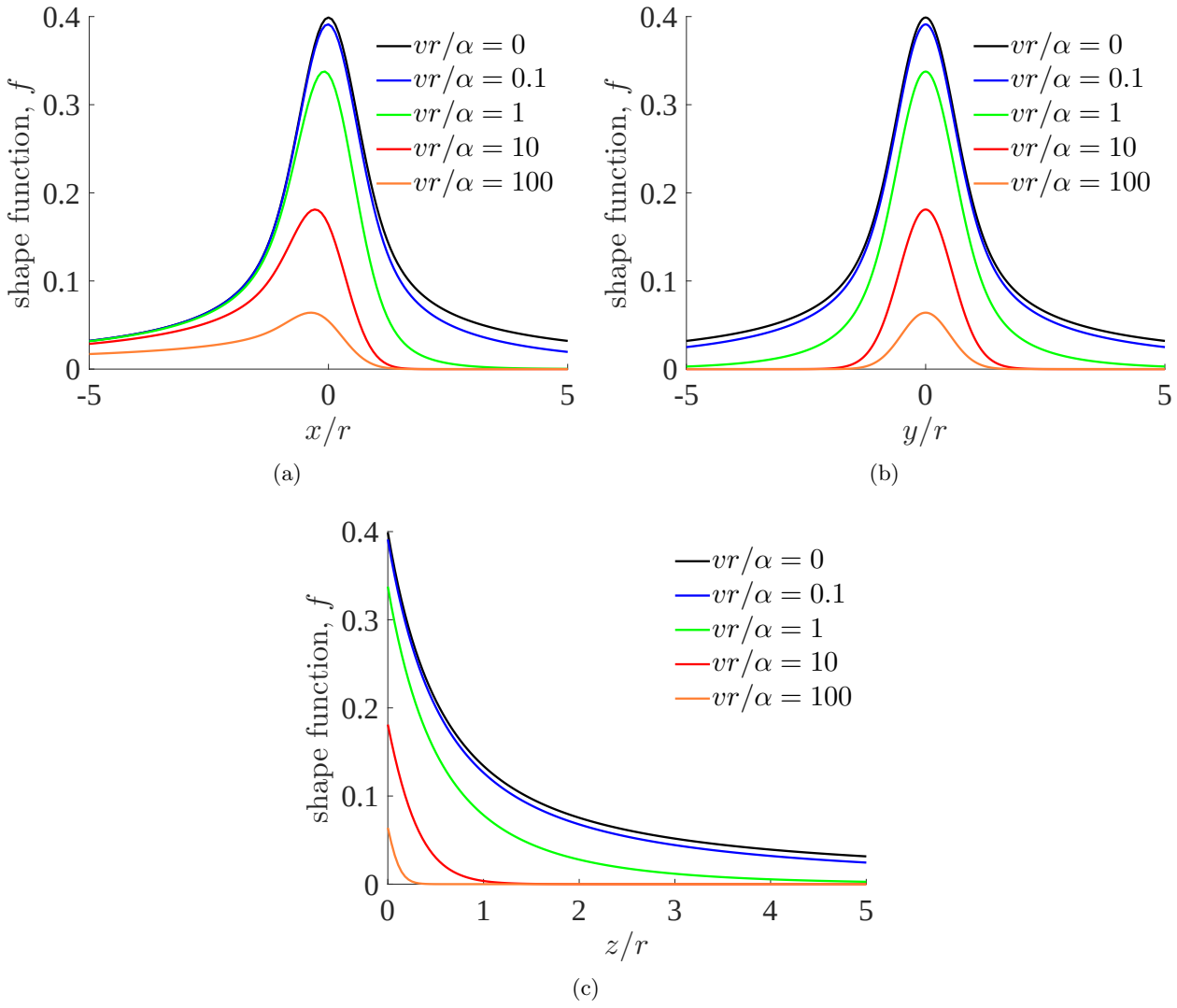

Figure 5. Plots of the shape function f that predicts the distribution of temperature in the powder bed as a function of dimensionless velocity, $\overline{v} = v\,r/\alpha$: (a) Along the x-axis, the direction of laser travel, the peak temperature lags behind the location of the beam ($x = 0$); (b) Along the y-axis, the temperature distribution is symmetric; (c) Along the z-axis, f predicts the depth of penetration of the temperature disturbance. As $\overline{v}$ decreases, f and thus the temperature distribution approach constant profiles.

Considering a powder bed composed of plain AlSi10Mg (Table 1), we now integrate over the surface to solve for $T(x, y, z = 0)$ as a function of laser power and scan velocity. Maintaining a constant areal energy density, $E_{\mathrm{A}} \equiv P/(v \cdot 2r)$, we plot the predicted temperature distribution at three different powers and velocities (Figure 6). Here, although the energy density is the same in each case, the melt pool dimensions, aspect ratio, and peak temperature increase with increasing scan velocity. Referring to the temperature solution (Equation 6), we note that the amplitude term increases linearly with increasing laser power, but the effect of increasing the scan velocity is hidden within the shape function (which includes an exponential term). Because Al-Si10-Mg has a high thermal diffusivity, $\alpha = 6.2 \times 10^{-5}\,\mathrm{m}^2/\mathrm{s}$, $\overline{v}$ is small at these scan velocities, ranging from $v\,r/\alpha = 0.32$ to $v\,r/\alpha = 1.28$. Therefore, as shown in Figure 6, the shape function hardly changes as the scan velocity increases in this range. With the amplitude term increasing linearly and the shape function remaining approximately constant, the temperature and thus the melt pool dimensions must increase as the laser power is increased at constant energy density.

The key result of this analysis is the nonlinear relationship between $\overline{v}$ and the distribution of temperature in the material. At constant laser intensity, when $\overline{v}$ decreases in the range of $\overline{v} = 1{-}100$, the maximum temperature in the material increases logarithmically, but thereafter there is little benefit in increasing $\overline{v}$. Similarly, the size of the melt pool, indicated by the width of the temperature distributions at a given value of f, does not increase significantly for $\overline{v} \lesssim 1$. This result explains the limitations in laser consolidation of increasing energy density by decreasing laser scan velocity. Rather, it is preferable to increase laser power, particularly for materials with high thermal diffusivity, such as aluminum alloys.

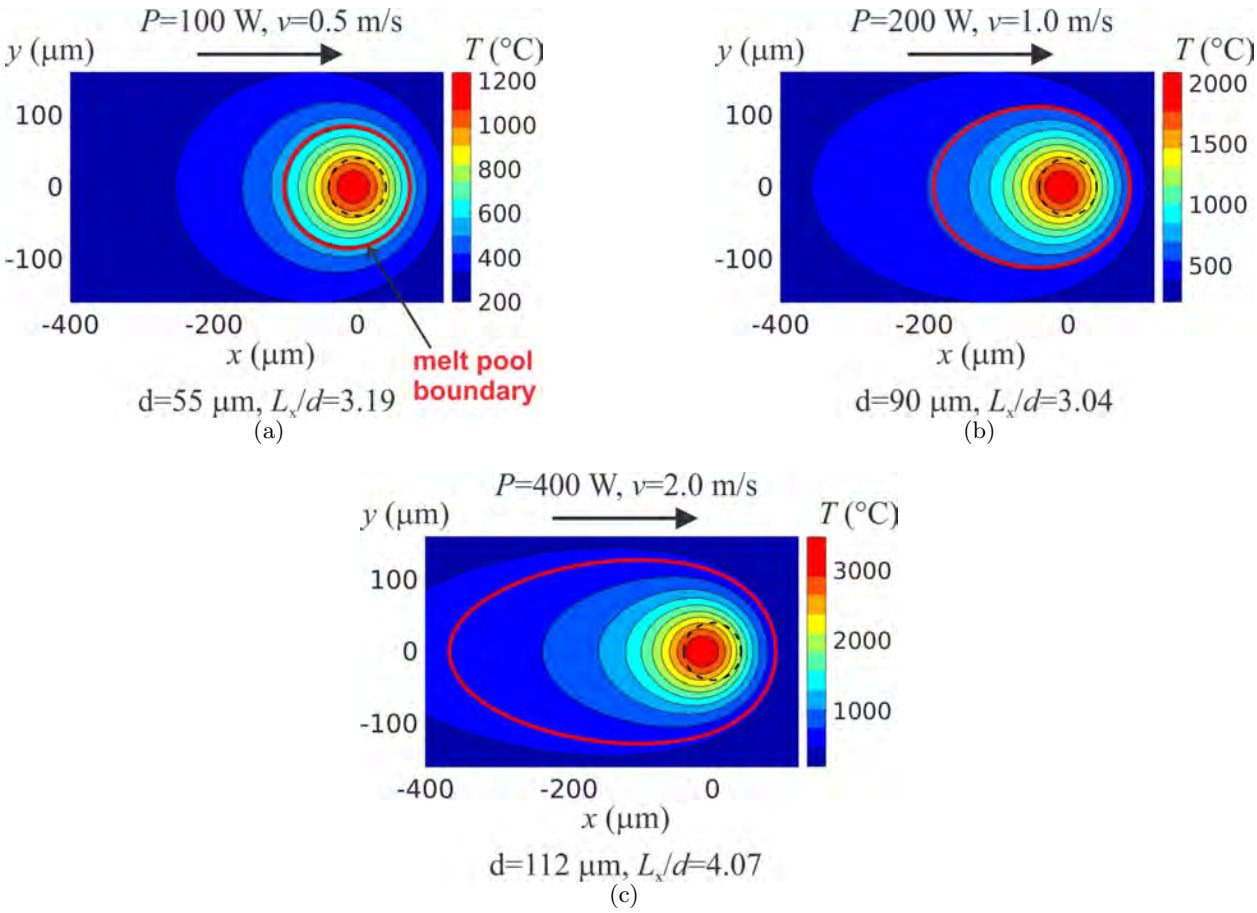

Figure 6. Analytic model predictions of melt pool size and temperatures $T(x, y, 0)$ for plain Al-Si10-Mg: Melt pool dimensions, aspect ratio, and maximum temperature increase with increasing laser scan velocity at constant areal energy density, E_A (for $d_{beam} = 80\ \mu m$ and $A = 0.35$): (a) $v\,r/\alpha = 0.32$; (b) $v\,r/\alpha = 0.64$; (c) $v\,r/\alpha = 1.28$. (Dashed circle indicates position of laser beam spot.)

TABLE 1

Physical Properties of AlSi10Mg

Powder density, ρ_{pow}	$1300\,\mathrm{kg/m^3}$
Consolidated density, ρ_{dens}	$2670\,\mathrm{kg/m^3}$
Powder thermal conductivity, k_{pow}	$10\ \mathrm{W/m\,K}$
Consolidated thermal conductivity, k_{dens}	$150\ \mathrm{W/m\,K}$
Specific heat c_{p}	$900\ \mathrm{J/kg\,K}$
(Thermal diffusivity, α)	$(1.28 \times 10^{-5} - 6.25 \times 10^{-5}\,\mathrm{m^2/s})$
Solidus temperature, T_ℓ	$558\,^{\circ}\mathrm{C}$
Liquidus temperature, T_{s}	$594\,^{\circ}\mathrm{C}$
Vaporization temperature, T_{v}	$2450\,^{\circ}\mathrm{C}$
Latent heat of fusion, L_{f}	$389\,\mathrm{kJ/kg}$
Effective absorptivity, A	0.35

This page intentionally left blank.

5. NUMERICAL MODELING OF LASER CONSOLIDATION

Analytical models and nondimensional groups can uncover fundamental relationships between process parameters, microstructure, and properties, but it is very difficult to derive analytical solutions for cases with finite geometry or modes of heat transfer in addition to pure conduction. On the other hand, numerical solutions can predict melt pool characteristics and thermal history under conditions far more complex than those of the idealized case of Section 4. Some of the phenomena that can readily be incorporated into numerical models are convective heat transfer, thermal radiation, phase changes, temperature dependence of material properties, and multiple scan tracks.

In the numerical solutions, the material is modeled at the continuum level, where the computational cost is reasonable, using the finite element method to solve the heat and momentum equations. While models of SLM have been proposed in the literature, there is still a critical need for comprehensive, numerically efficient models that capture the coupled physics of heat transfer and deformation. Reviewing the prior work, we identified opportunities in the following areas, among others:

- Efficient numerical schemes: adaptive time stepping, optimized element sizes, element activation, and elements with hybrid shape functions for u and T that are not prone to locking
- Realistic material models for compaction of powder and viscoplasticity of the solidified metal at elevated temperature
- Physical representations of melt pool convection and recoil pressure based on non-local field variables defined by dimensional analysis
- Benchmarking of numerical methods and modeling assumptions with analytical solutions and the results of experiments
- Massive parallelization using resources at the LL Supercomputing Center

For FY 2018, the objective was to develop accurate, efficient models of the heat transfer process. To this end, first, the analytical solution of Section 4 was derived. Then, a numerical model of the pure conduction problem was built for solution by the commercial finite element solver Abaqus (Dassault Systemes). In the numerical model, the intensity of the laser beam is described by the same Gaussian form previously given by Equation 1. The preprocessing and postprocessing of all numerical simulations were scripted in Python so that parametric studies could be readily performed. With this capability, we can easily run multiple simulations in order to identify trends associated with single or groups of process parameters. As such, the detailed physics of SLM can be simulated nearly as easily as it can be with an analytical model.

5.1 NUMERICAL INTEGRATION SCHEMES

A critical step in developing a numerical model is to determine a domain size and level of discretization that provide an optimum balance between accuracy and computational cost. In general, these parameters depend on the properties of the material being modeled, and here we focus on AlSi10Mg (with physical properties given in Table 1). In these initial numerical simulations, the material properties are approximated to be independent of temperature and the effects of phase changes are neglected so that the predictions can be directly compared with those of the analytical model. For process parameters, we select the typical parameters used for AlSi10Mg with an EOS M 290 SLM machine (Table 2).

TABLE 2

Typical SLM Process Parameters for AlSi10Mg

Laser power, P	370 W
Laser scanning speed, v	1.3 m/s
Layer thickness, t	40 μm (effective)
Beam radius, r	50 μm
Hatch spacing, h	190 μm
Initial temperature, T_0	20 °C

For AlSi10Mg, parametric studies of single track consolidation were carried out to determine the optimum geometry of the simulation domain and the appropriate number of solution points within this domain. Based on the analytical predictions of the size of the heat-affected zone, the domain size was chosen to be $L_x = 1.52$ mm, $L_y = 0.8$ mm, and $L_z = 0.4$ mm (Figure 7). This domain was discretized with 8 node linear heat transfer elements (Abaqus DC3D8). Simulating single track consolidation with decreasing element size, we found that the analytical solution for the steady state temperature distribution could be matched with an element size of $h \approx 20$ μm, or about one-fifth of the diameter of the laser beam (Figure 8a). Furthermore, with this element size, the transient numerical solution approaches the steady state analytical solution after a scan length of only $L_{\text{scan}} = 0.60$ mm (Figure 8b), verifying that the overall length of the domain, L_x, is sufficient. Considering the size of the heat-affected zone (Figure 7), we estimate that the width and depth of the domain could each be decreased in size by about 33%. Summarizing the spatial requirements, a domain volume of about 0.25 mm^3 and about 14,000 linear finite elements are adequate to simulate single track consolidation of AlSi10Mg under typical SLM conditions.

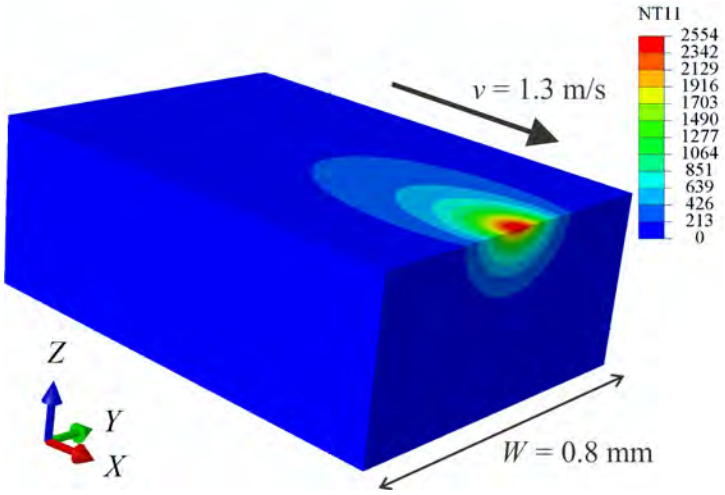

Figure 7. Numerical simulation of single track consolidation of plain AlSi10Mg at scan length $L_{\text{scan}} = 0.6\,mm$ ($P = 370\,\text{W}$, $v = 1.3\,\text{m/s}$, $d_{\text{beam}} = 100\,\mu m$, $A = 0.35$, and element size $h = 10\,\mu m$).

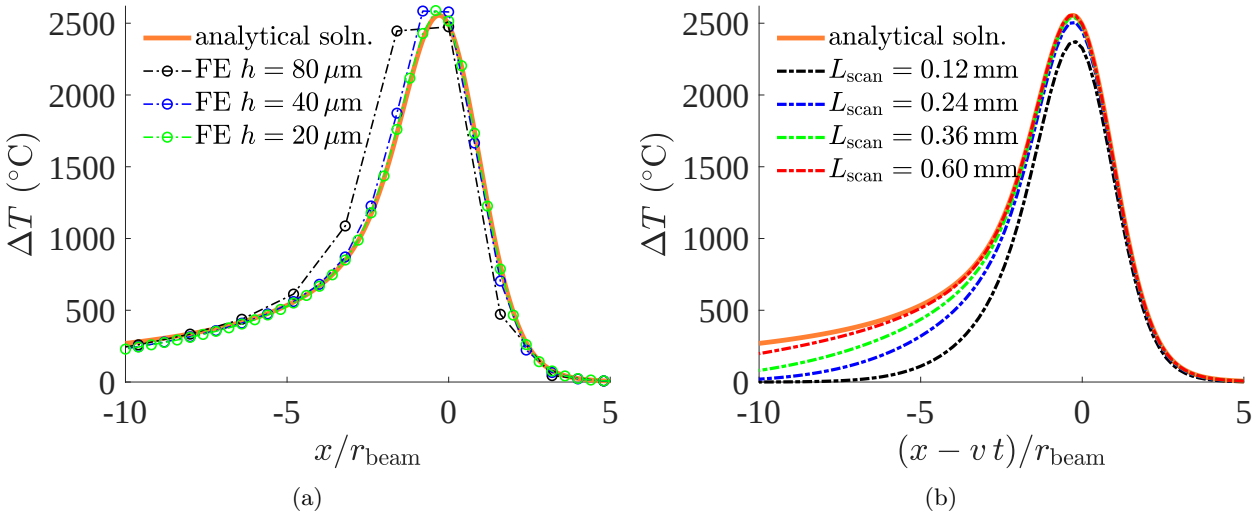

Figure 8. Comparison of the melt pool temperatures predicted by analytic and numerical models as a function of element size (a) and laser scan length (b). Steady state analytic solution is approached at $h = 20\,\mu m$ and $L_{\text{scan}} = 0.60\,mm$.

Like the spatial integration scheme, the time integration scheme was also optimized in order to minimize solution time. In another parametric study, with $h = 20$ μm and $L_{\text{scan}} = 0.72$ mm, the

effect of increasing the maximum incremental temperature change was investigated. The results show that the time increment can be increased to a length that allows changes in temperature as long as $\Delta T_{\text{incMax}} = 400\,^{\circ}\text{C}$ during a single time increment, without significantly affecting the prediction of the steady state temperature distribution (Figure 9). This time increment reduces the total simulation time by a factor of 12, compared to the time increment corresponding to the initial guess of $\Delta T_{\text{incMax}} = 25\,^{\circ}\text{C}$.

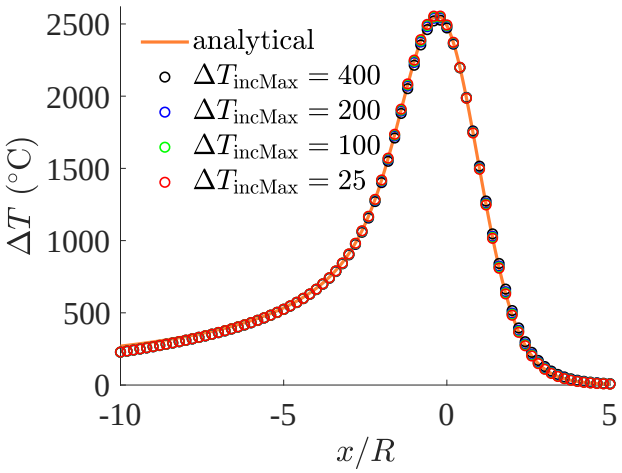

Figure 9. Comparison of the melt pool temperatures predicted by analytic and numerical models as a function of the size of the time increment used in the time integration scheme. Time increments that allowed the temperature to change by as much as 400 °C still produced an accurate solution. ($h = 20\,\mu m$ and $L_{\text{scan}} = 0.72\,mm$.)

5.2 ALGORITHM FOR MATERIAL PHASE CHANGES

With the numerical solution methods benchmarked and optimized, the numerical model was extended to capture changes of material phase. At each time step in the simulation, the material at each integration point in the domain is described by three state variables: the material phase (powder, consolidated solid, or liquid metal), the volume fraction of dense material (including both liquid and consolidated solid), and the maximum temperature at that point during the current total simulation time (Table 3). AlSi10Mg, like most alloys, melts and solidifies over a range of temperature called the "mushy" zone, $T_{\text{s}} \leq T \leq T_{\ell}$, where T_{s} is the solidus temperature and T_{ℓ} is the liquidus temperature. The material therefore melts and solidifies gradually, avoiding the numerical instability that would occur if the change of phase happened abruptly at a single temperature. The

volume fraction of dense phase is given by

$$\phi = \begin{cases} 0 & \text{if} \quad T \leq T\text{s}, \\ \dfrac{T - T_\text{s}}{T_\ell - T_\text{s}} & \text{if} \quad T_\text{s} < T < T_\ell, \\ 1 & \text{if} \quad T \geq T_\ell, \end{cases} \tag{7}$$

under the constraint $\dfrac{\mathrm{d}\,\phi}{\mathrm{d}\,T} \geq 0$ because densified material, whether liquid or solid, cannot spontaneously transform back to powder. Initially, before the arrival of the laser beam, the material is powder (iPhase=1), but, when the temperature exceeds T_ℓ, it changes to liquid (iPhase=3). Once the material is liquid and the temperature then decreases below T_s, the liquid transitions to consolidated solid (iPhase=2).

TABLE 3

Variables in Numerical Model Describing Material State

State variable	**Description**	**Values**
iPhase	Material phase	1 – Powder 2 – Consolidated solid 3 – Liquid
ϕ	Volume fraction of dense phase	$0 - 1$
T_max	Maximum temperature reached at material point	$T_0 - \infty$

Associated with the phase changes are latent heat effects and the dependence of the material properties on temperature. The latent heat of fusion is incorporated by increasing the specific heat capacity when the temperature is between T_s and T_ℓ:

$$c_\text{p} = \begin{cases} c_\text{p,sensible} & \text{if} \quad T \leq T\text{s}, \\ c_\text{p,sensible} + \dfrac{L_\text{f}}{T_\ell - T_\text{s}} & \text{if} \quad T_\text{s} < T < T_\ell, \\ c_\text{p,sensible} & \text{if} \quad T \geq T_\ell. \end{cases} \tag{8}$$

The thermal conductivity and mass density of the material are related to the temperature through their dependence on the volume fraction of dense phase:

$$k = k_{\text{pow}} \; + \; \phi \times (k_{\text{dens}} - k_{\text{pow}}) \,, \tag{9}$$

and

$$\rho = \rho_{\text{pow}} \; + \; \phi \times (\rho_{\text{dens}} - \rho_{\text{pow}}) \,, \tag{10}$$

where $k_{\text{pow}} \ll k_{\text{dens}}$ and $\rho_{\text{pow}} \approx 1/2\, \rho_{\text{dens}}$ (Table 1).

5.3 PREDICTIONS OF THE NUMERICAL MODEL WITH MATERIAL PHASE CHANGES

Adding these effects to the numerical model significantly changes the distribution of temperature and the dimensions of the melt pool (Figure 10). Here, we simulated a 40 μm layer of AlSi10Mg powder spread on a build plate of AlSi10Mg. The low thermal conductivity of the powder surrounding the heat-affected zone insulates the melt pool, causing the melt pool to increase in size and temperature, relative to the predictions of the simulation without phase changes. Similarly, the insulating effect of the powder decreases the width of the heat-affected zone and reduces its extent in the scan direction. Conversely, the length of the tail of the heat-affected zone increases because the consolidated material left in the wake of the melt pool has high thermal conductivity (Figure 11).

As a whole, the predictions of the numerical model are consistent with the formation of stable melt pools and the consolidation of defect-free parts. The predicted melt pool measures about 380 μm long, 160 μm wide, and 100 μm deep. A melt pool of these dimensions is expected to be stable because it avoids the capillary instability that occurs in liquid cylinders with $L/d > \sqrt{3/2}\,\pi$. Furthermore, it is also deep enough to remelt over 50 μm of the build plate, ensuring a good connection between the layers in a build. The maximum temperature predicted, about 2700 °C, exceeds the vaporization temperature of aluminum, indicating that the metal will vaporize at the surface of the melt pool. However, vaporization is common in SLM and is not a concern unless it causes a significant change in the elemental composition of the alloy.

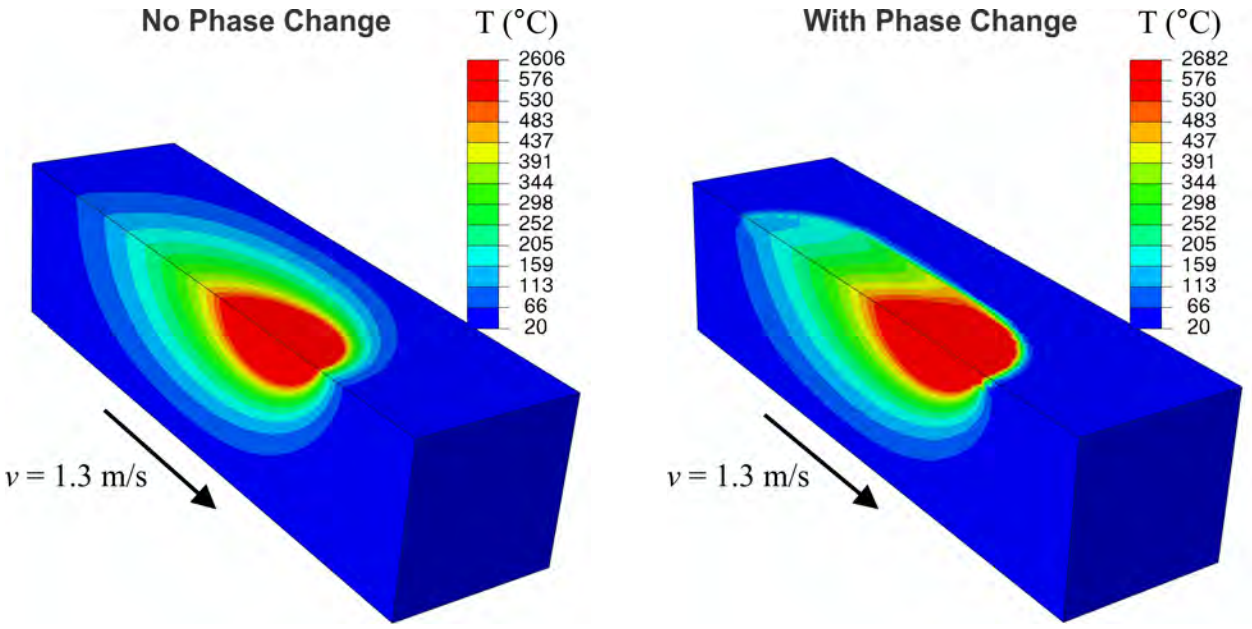

(a) (b)

Figure 10. Numerical simulations showing the effect of material phase changes and the temperature dependence of material properties on the prediction of the steady state temperature distribution for AlSi10Mg. The phase changes and accompanying change in material properties increase the melt pool temperature and dimensions but decrease the size of the heat-affected zone. ($h = 20\,\mu m$ and $L_{\text{scan}} = 0.72\,mm$.)

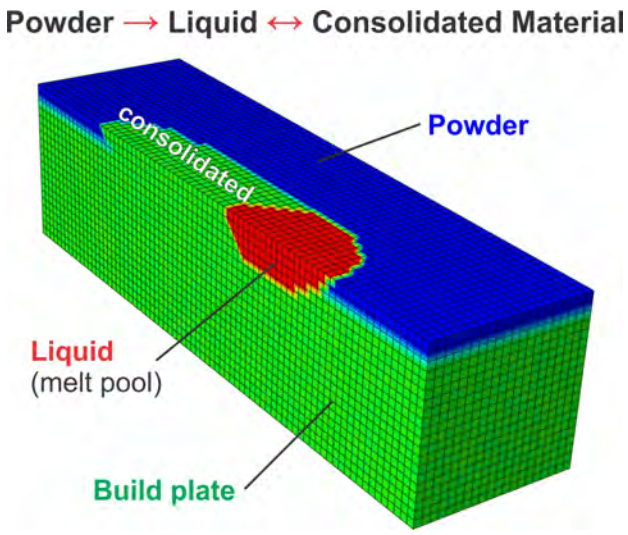

Figure 11. Distribution of material phases for the simulation of AlSi10Mg shown in Figure 10. ($h = 20\,\mu m$ and $L_{\text{scan}} = 0.72\,mm$.)

6. CONCLUSION

During FY 2018, we developed accurate, efficient models of the heat transfer and phase changes that occur during selective laser melting. First, the exact analytical solution was derived for the steady state temperature distribution generated by a scanning Gaussian intensity source. Next, a numerical model of the conduction problem, scripted for parametric studies, was developed and verified with the analytical solution, and the effects of model size, scan length, element size, and time step were investigated. Surprisingly, we found that the analytical solution can be approximated numerically with an element size as large as about one-quarter of the beam diameter and model dimensions on the order of 1 mm. The numerical model was then extended to simulate more detailed physics, including phase changes and temperature dependence of material properties. Agreeing with our intuition, these effects increase the temperature and dimensions of the melt pool, and the predictions are consistent with the melt pool characteristics of successful SLM builds.

In FY 2019, the focus will shift to modeling multiple layers and the coupled structural mechanics problem. Mechanical loads and melting cause powder to compact, and the high temperatures and thermal cycling of SLM activate creep mechanisms. Therefore, unlike prior efforts, we will develop and implement accurate material models of the elastic-plastic responses of the powder and the fused material. Modeling both elastic and plastic deformation is essential for prediction of part distortion and residual stresses. Initially, simulations will be conducted with the commercial solver Abaqus because its solution methods are highly efficient, all model definitions and job executions can be scripted in Python for parametric studies, and it provides numerous subroutines for user definition of elements, material models, boundary conditions, and field variables that can be readily ported to other solvers. Because these simulations may become computationally expensive, we will also transfer these subroutines to an open source solver that can be parallelized over 100+ cores at the MIT LL Supercomputing Center (e.g., Sierra or FEAP).

The development of internal process modeling capability will ensure that MIT LL remains at the forefront of metals AM. Prediction of melt pool characteristics and thermal history will enable the processing of alloys with yield strength, fatigue strength, and ductility superior to those of existing AM alloys. Defects, distortion, and residual stresses can be predicted and prevented by tuning process parameters, thereby expediting part qualification. Furthermore, there is recent interest in leveraging MIT LL's core expertise in sensing, imaging, and data processing to integrate high resolution temperature measurement with SLM. Because only surface measurements of temperature can be made, models of the process will then be indispensable in the development of algorithms that can use surface temperatures to predict defects that form below the surface and enable real-time forward control of process parameters.